Theoretical Study and Device Modeling of III-V Nanostructured Photovoltaics

Ryan Aguinaldo
Nanopower Research Laboratories, Dept. of Microelectronic Engineering, and Center for Materials Science and Engineering
Rochester Institute of Technology, Rochester, NY 14623. Email: rfa1484@rit.edu

Abstract – **A methodology for the modeling and theoretical analysis of novel nanostructured photovoltaic devices is presented in this work. The nanostructures in consideration are quantum wells and quantum dots composed of III-V materials. Their incorporation into the space charge region of an otherwise conventional solar cell is presented as a means to increase photovoltaic energy conversion efficiency. The enhancement for both single- and multi-junction solar cells is also outlined. Limitations of the available models are briefly discussed. Analyzed results allow for the further optimization of these novel devices.**

I. Introduction

The efficiency of a single-junction, crystalline solar cell is limited by the laws of thermodynamics to a maximum efficiency of approximately 30% under one-sun illumination [1] and approximately 40% under full solar concentration [2]. Using a multi-junction approach, the efficiency of state-of-the-art crystalline photovoltaics has recently surpassed 40% under solar concentration [3]. Although impressive in its own right, this number is nowhere close to the theoretical maximum for such a device. Detailed balance calculations indicate that the bandgap of the middle junction in this type of architecture is slightly larger than ideal thus causing it to be the limiting component within the device stack [4].

The use of low-dimensional nanostructures provides a means to introduce a smaller bandgap material into the otherwise non-ideal device structure thus increasing photovoltaic efficiency. Additionally, the incorporation of nanostructures has been proposed in the literature as a viable way to increase the efficiency of single-junction cells by the absorption and photoconversion of sub-bandgap photons. In this work, the term nanostructures refers to quantum wells and quantum dots.

Nanostructured solar cells are being fabricated at the Rochester Institute of Technology. The development of such devices requires a fundamental understanding of the nanostructure arrays, the behavior of such structures within a single- or multi-junction solar cell, and a means to predict the operational performance of these devices. Therefore, it is the purpose of this work to develop theoretical methodologies that adequately describe the performance of fabricated devices and that are able to gauge the necessities for future device architectures.

The main focus of this work is to evaluate the ability to use a commercially available physics-based model to describe the operation and internal physics of these nanostructured devices. Additionally, bandstructure calculation of the nanostructure superlattices are also performed to give further insight into the internal workings and further optimization of nanostructured photovoltaic devices. The materials systems present here will focus on the InAs/GaAs (confined/device) system.

II. Motivation

The conversion efficiency of a traditional single-junction solar cell is limited by the bandgap of the material used to make the device. The light output of the sun is made up of a wide range of wavelengths corresponding to a wide range of photon energies. However, photons with energies less than that of the bandgap in consideration are not absorbed by the device and thus do not contribute to photogeneration of charge carriers. As an example, the air-mass zero (AM0) solar spectrum [5] is shown in Fig. 1 with useful and non-useful regions for solar energy conversion for a GaAs solar cell. Additionally, the most efficient conversion of photons into free charge carriers occurs at the bandgap. Higher energy photons will exhibit a lower degree of photoconversion efficiency.

The incorporation of either quantum wells [6] or quantum dots [7] have been proposed as a method to absorb some of the otherwise wasted radiation. This in turn will increase photovoltaic efficiency of a single-junction device and serves as a motivation for this work.

Another method employed to make better use of the solar spectrum is by the use of a multi-junction architecture. In this scheme, several p-n junctions, each composed of a different material, is grown in tandem. This type of device is optimized by placing the largest bandgap junction as the top cell and by making each subsequent junction of a smaller bandgap material. In this sense, the highest energy photons (those which are quickly absorbed) are efficiently photoconverted while sub-bandgap photons, being transparent to one junction, propagate further down through the stack until they are able to be absorbed.

The state-of-the-art lattice-matched cell is the InGaP-GaAs-Ge stack as seen in Fig. 2.a. The useful regions of absorption corresponding to each stack are illustrated in Fig. 2.b. A similar scheme has recently been employed to

demonstrate 40% conversion efficiency under 240 sun solar concentration [3].

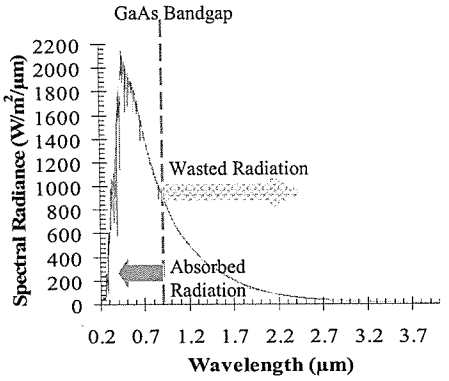

Fig. 1. AM0 solar spectrum. The GaAs bandgap (1.42 eV), as an example, is placed on the plot to split the spectrum into regions that are usable and unusable for photoconversion by a GaAs cell. Additional inefficiencies, not shown on the diagram, will occur for higher energy photons.

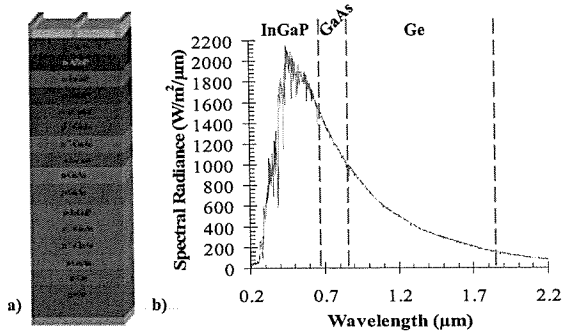

Fig. 2. a) The triple-junction InGaP-GaAs-Ge solar cell. b) The AM0 solar spectrum showing regions of absorption corresponding to the materials used in the triple-junction stack.

Extending upon the detailed balance formulation [1], [4], the calculation of solar efficiency can be shown to be dependent on the flux of absorbed photons with energies greater than the semiconductor bandgap E_g:

$$\phi_S = \frac{2\pi}{h^3 c^2} X f_\Omega \int_{E_g}^{\infty} \frac{\varepsilon^2 d\varepsilon}{e^{\varepsilon / k_B T_S} - 1} \tag{1}$$

and the flux of radiative emission:

$$\phi_C = \frac{2\pi}{h^3 c^2} \left[\int_{E_g}^{\infty} \frac{\varepsilon^2 d\varepsilon}{e^{(\varepsilon - qV)/k_B T_C} - 1} - (1 - X f_\Omega) \int_{E_g}^{\infty} \frac{\varepsilon^2 d\varepsilon}{e^{\varepsilon / k_B T_S} - 1} \right] \tag{2}$$

where h is Planck's constant, c is the speed of light, q is the elementary charge, V is the applied bias, k_B is Boltzmann's constant, T_S is the temperature of the sun, T_C is the temperature of the device, X is the number of suns for solar concentration, and $f_\Omega = \Omega/\pi \approx 2.16\times10^{-5}$ is a geometrical factor based on the solid angle Ω subtended by the sun with respect to a planar solar cell. Efficiency is thus given as

$$\eta = \frac{qV(\phi_S - \phi_C)}{P_S} \tag{3}$$

where P_S is the solar constant.

For a multi-junction cell, each junction will be imbued with the quantity (ϕ_S - ϕ_C); however, due to the constraint of current-matching, this quantity must be equal for each specific cell. This determines the potential across each junction. For the InGaP-GaAs-Ge cell under one sun blackbody illumination, the maximum efficiency is calculated to be approximately 33%. Figure 3 shows a plot of triple junction iso-efficiency contours as a function of the bandgaps of the top two junctions. The bottom cell bandgap is fixed to that of Ge (0.67 eV). As the plot indicates, decreasing the middle junction from that of GaAs (1.42 eV) to 1.2 eV yields an increase in the maximum efficiency of the triple-junction cell from 33% to 47%. This is not easily accomplished by traditional means because there is no material with this bandgap that is lattice matched to Ge and InGaP. The incorporation of nanomaterials, however, provides for an effective decrease in bandgap thus serving for an additional motivation for this work.

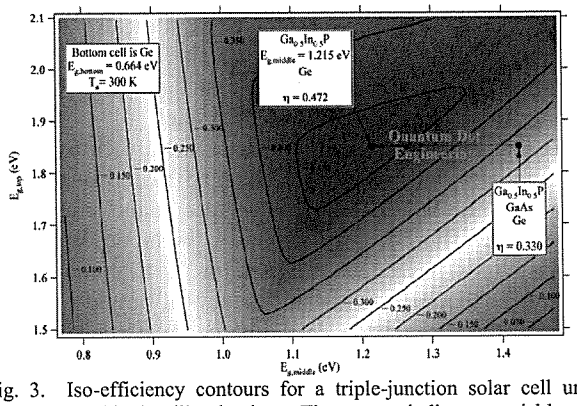

Fig. 3. Iso-efficiency contours for a triple-junction solar cell under 6000 K blackbody illumination. The axes indicate variable cell bandgaps. The state-of-the-art GaInP/GaAs/Ge cell is shown at 33% efficiency. Replacing the GaAs middle junction with a hypothetical material of 1.2 eV bandgap increases the cell efficiency to 47%. This serves as a motivation for bandgap engineering by way of nanostructures.

III. NANOSTRUCTURES

When the size of a system is on the order of the de Broglie wavelength, quantum mechanical effects are realized. In the case of semiconductor heterostructures, a

thin layer of a smaller bandgap material sandwiched between a larger bandgap material may form a quantum well. In this sense, the smaller bandgap material forms a potential well for charge carriers. In this well, energy levels are quantized. The band diagram is drawn for an array of quantum wells in Fig. 4. If quantum confinement occurs in all three spatial dimensions then a quantum dot is formed. An atomic force micrograph of InAs quantum dots grown on a GaAs substrate is shown in Fig. 5.

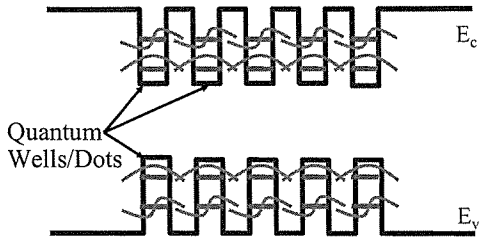

Fig. 4. Band diagram of a quantum well/dot array. A smaller bandgap material placed in a host material of larger bandgap creates potential wells for charge carriers. Quantization of energy levels occurs in these wells. Electron and hole wavefunctions are superimposed over the energy levels.

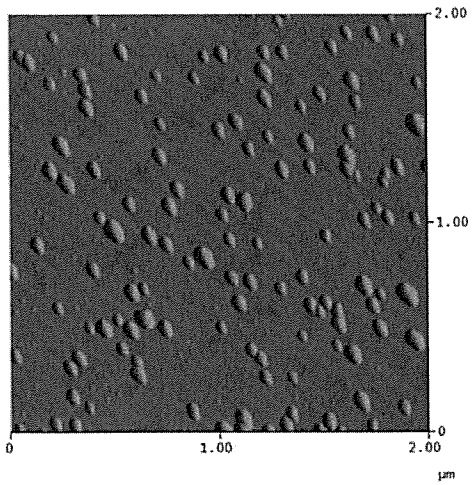

Fig. 5. Atomic force micrograph of InAs quantum dots grown on a GaAs substrate. Average quantum dot height is 6 nm. Such structures are grown by metal-organic vapor phase epitaxy.

From Fig. 4, it is easy to see that the incorporation of a nanostructure array within a host material allows for additional absorption mechanisms. Sub-bandgap photons which are not absorbed by the host material may be absorbed by the nanostructures thus increasing solar cell efficiency. Also, due to the fact that the introduced energy transitions represent smaller energies than the host bandgap, an effective bandgap decrease may be realized for the case of increasing the efficiency of the triple-junction cell as previously discussed.

In Fig. 4, eigenfunctions are drawn for each of the quantized energy levels. For thick barriers (i.e. the host material between adjacent quantum wells), the eigenfunctions resemble that of an isolated quantum well. Decreasing the barrier thicknesses, such that non-negligible overlap of carrier wavefunctions occurs, leads to the formation of minibands as diagramed in Fig. 6. This allows for additional absorption and carrier transport mechanisms. A periodic array of quantum wells or quantum dots thus forms a superlattice in the sense that a periodic array of atoms forms a traditional crystal lattice. Miniband formation is necessary in the theory of the intermediate band solar cell [7], [8].

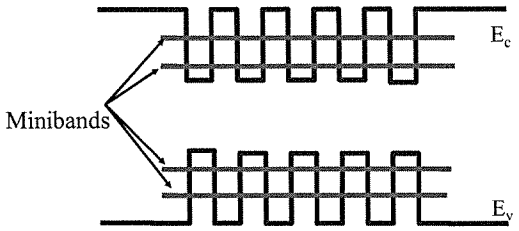

Fig. 6. Band diagram of a quantum well/dot array. A smaller bandgap material placed in a host material of larger bandgap creates potential wells for charge carriers. Non-negligible overlap of electron and hole wavefunctions, as seen in Fig. 4, induces the formation of minibands. A superlattice is formed for a periodic area of closely spaced quantum wells/dots.

IV. Device Modeling

A. Simulation Methodology

The modeled device is a GaAs p-i-n solar cell as seen in Fig. 7. The presence of a thin intrinsic region serves to increase the depletion width. Additionally, the nano-structure array is centered within the i-layer. The InGaP window and back surface field (BSF) reflect minority carriers towards the junction.

The device is modeled as a two-dimensional structure as shown in Fig. 7.a. Additionally, only one grid finger of the solar cell is simulated. These approximations keep computation time to a minimum. After calculations are completed, geometrically dependent results, such as current, are multiplied by a scaling factor that accounts for the three-dimensional nature of an actual device; this simulates the device structure as seen in Fig. 7.b. Finally, another multiplication factor is included to account for the desired number of grid fingers; this simulates the structure in Fig. 7.c and is comparable to an experimental device.

The Silvaco Atlas software package is utilized for the device simulations. Silvaco Atlas is a physics-based device simulator that numerically solves coupled Poisson and continuity equations by iteration. Additional models are included and invoked as necessary. Due to the relatively large dopings encountered throughout the simulated device, Fermi-Dirac statistics are used to determine carrier concentrations. Shockley-Reed-Hall and radiative recombination models are also invoked.

Additional recombination is handled at the hetero-interfaces and the terminal surface. Thermionic emission is also accounted for at the InGaP-GaAs interfaces. Photogeneration of charge carriers is modeled using AM0 illumination.

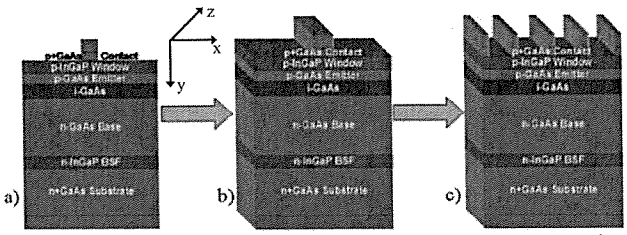

Fig. 7. The solar cell is modeled as a) a two-dimensional structure using only one grid finger. These approximations keep computation time to a minimum. Final results that are dependent on geometry, e.g. current, are modified by a scaling factor to account for b) the three-dimensional nature of an actual device. An additional factor is included to c) account for the desired number of grid fingers to make the model comparable to an actual device.

For the simulation of a nanostructured device, an InAs quantum well array is centered within the i-region of Fig. 7. This is done to simulate the InAs quantum dot solar cells that are being fabricated at the Rochester Institute of Technology. The justification for using the quantum well model in the device simulation is that this model calculates quantum confinement only in the y-direction (referring to Fig. 7). In the actual device, the quantum dots are more strongly confined in the y-direction; this is also the direction of current flow. Thus the use of the quantum well model to approximate a quantum dot array is justified.

While invoking the quantum well model, the effective mass Schrödinger equation is numerically solved in and around quantum confined regions. The solution gives energy eigenvalues for further use in bandstructure-dependent optoelectronic models to be discussed. Corresponding eigenfunctions are also determined as part of the solution.

The bandstructure-dependent optoelectronic models incorporated in Atlas use the results from the quantum well model to determine the effects of optical gain and spontaneous emission [9]. These effects are useful for laser and LED simulations, respectively. They do not, however, adequately describe quantum mechanical photogeneration of electron and holes. What would be necessary is a model that emulated or solved the selection rules which govern carrier transitions determined from Fermi's golden rule. An appropriate model for quantum mechanical photogeneration has not been identified.

B. Results

A baseline device, i.e. one without a quantum well array, was simulated and gave a close match to an experimentally fabricated baseline device. The purpose for doing this was to confirm validity of the device simulator with a conventional device; once confirmed, a novel device may be simulated with impunity. Both the simulated and empirical device resulted in a short circuit current I_{sc} just under 25 mA/cm^2 and an open circuit voltage $V_{oc} = 1.04$ *V*. The quantum well device exhibited slightly better device characteristics ($I_{sc} = 26.8$ *mA/cm*^{2}, $V_{oc} = 1.05$ *V*) but nowhere near the expected enhancement for either an ideal quantum well [6] or quantum dot [7] cell. Current-voltage characteristics of the fabricated device and the two simulation types are plotted in Fig. 8.

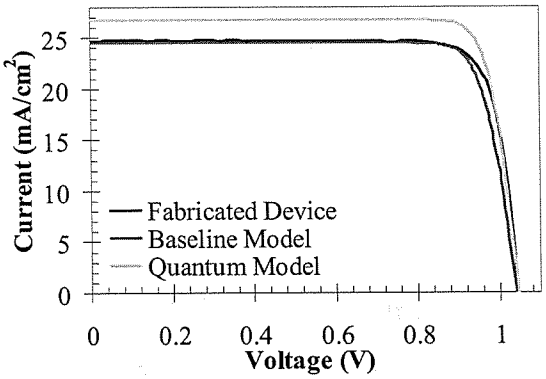

Fig. 8. Current-voltage characteristics for the fabricated baseline device and model and quantum well model. The baseline model gives a close match to experiment thus allowing for the further simulation of novel devices. The quantum well model gives a slight improvement in the device characteristics but not to the degree expected for such a device.

Analysis of the quantum efficiencies of the discussed examples, as in Fig. 9, gives information regarding the spectrally-dependent device response. For the baseline comparison, although the model underestimates the red response of an actual device, it overestimates the blue response thus accounting for the close match as seen in Fig. 8. As for the quantum model, sub-bandgap absorption is observed, however, characteristic peaks corresponding to quantized energy transitions are not. These peaks are commonly observed in quantum well [10] and quantum dot [11], [12] solar cells. The reason for not observing these peaks is as was discussed regarding the lack of an appropriate model that handles quantum mechanical photogeneration.

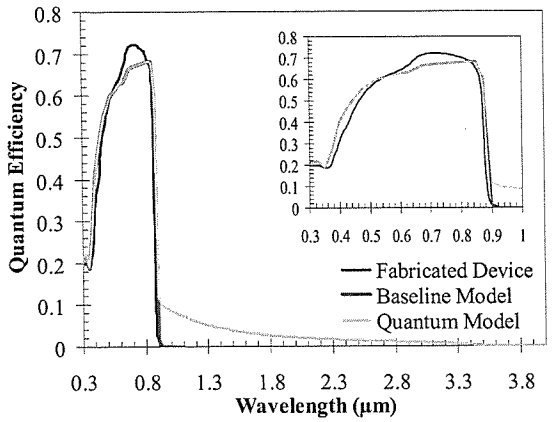

Fig. 9. Quantum efficiencies for the fabricated baseline device and model and quantum well model. In comparison to the fabricated baseline device, the baseline model underestimates the red response but overestimates the blue response thus leading to the match observed in Fig. 8. The quantum well model allows for sub-bandgap absorption; however, characteristic peaks due to the quantized energy transitions are not realized.

In lieu of obtaining the desired electrical results from the quantum well model, the analysis may be focused on the fundamental physics of the nanostructured device. The simulated band diagram in the nanostructured region of the quantum model is shown in Fig. 10. Calculated energy eigenstates are plotted within the InAs wells. For the system plotted, a single eigenstate occurs in the InAs conduction band and five heavy hole states and a single light hole state is realized in the InAs valance band. Also plotted is the wavefunction corresponding to the InAs conduction band eigenstate. This type of analysis is paramount in the research because the results summarized in Fig. 10 constitute values that cannot be directly measured experimentally but that lead to a better understanding of the device and its further development.

In the modeling that lead to Fig. 10, the well thickness was chosen to match the average height of the of quantum dots analyzed in Fig. 5; the barrier thickness was chosen because it allows for non-negligible wavefunction overlap. Based on the model, for 6 nm InAs wells, non-negligible wavefunction overlap occurs in the conduction band for approximately 8 nm barriers and thinner. Therefore, for this specific system, an 8 nm barrier thickness represents the threshold necessary to induce miniband formation. A plot of the wavefunctions for 10 nm and 7 nm barriers is given as an example in Fig. 11. In this plot, the 7 nm wavefunction can be seen to overlap throughout the well region while the 10 nm wavefunction does not.

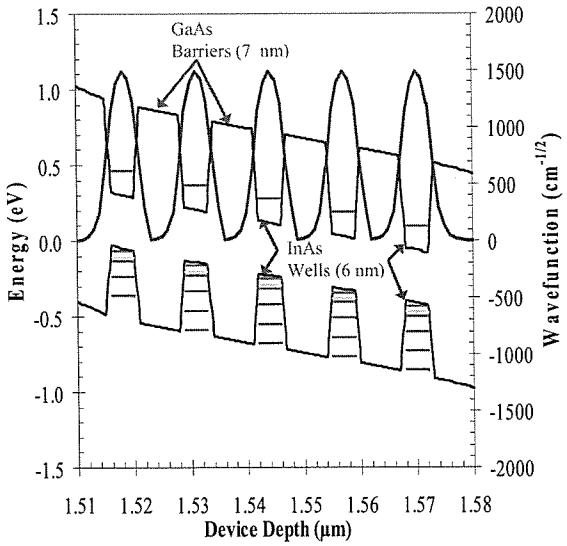

Fig. 10. Simulated band diagram of InAs confined regions within the space charge region of a GaAs solar cell. A single eigenstate is realized in the InAs conduction band due to quantum confinement. The corresponding wavefunction is superimposed. A second eigenstate is not realized due to the proximity of the band maximum to the GaAs continuum (~0.59 eV, see: Fig. 12). Also plotted are several heavy hole levels and a single light hole level (light green).

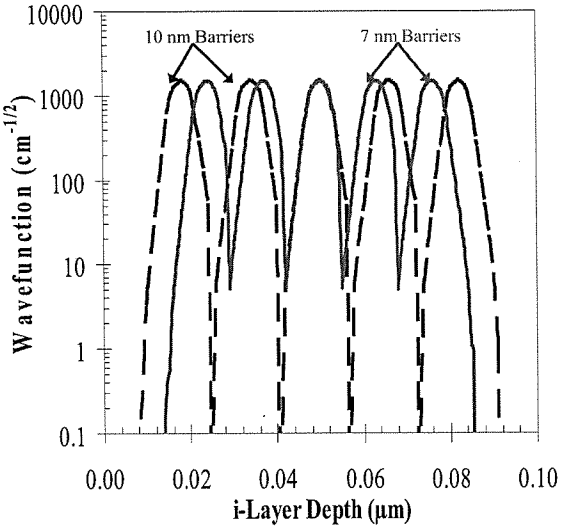

Fig. 11. Comparison of the conduction band bound state wavefunction for 10 nm barriers and for 7 nm barriers. In the 10 nm case, the wave function overlap is negligible. For the 7 nm case, a substantial amount of wavefunction overlap does incur; this leads to the formation of a miniband.

V. Bandstructure Calculations

In the previous section, results were interpreted arguing for the formation of a superlattice miniband. Exact information regarding the miniband is necessary to confirm the Atlas results as well as to take advantage of it in a photovoltaic device. One such way of determining

this information is by calculation of the superlattice bandstructure.

Bandstructure calculations for the InAs/GaAs superlattice are performed by invoking the Kronig-Penny model. This model approximates the crystal potential to be in the form of a periodic square potential. Although a poor approximation for a real crystal, this model proves to be an excellent choice of the superlattice since the band edges are in the approximated form.

The textbook example of the Kronig-Penny model is derived from the Schrödinger equation [13]:

$$-\frac{\hbar^2}{2m}\nabla^2\psi + U\psi = E\psi \tag{4}$$

where $\hbar$ is the reduced Planck's constant, m is the particle mass, U is the potential energy, E is the energy eigenvalue, and ψ is the eigenfunction. For a semiconductor superlattice, U is set equal to the band edge and m is replaced by the effective mass m^*. As a caveat, the effective mass in a superlattice becomes spatially dependent due to the presence of different materials. Thus the kinetic energy operator

$$T = -\frac{\hbar^2}{2m^*}\nabla^2 \tag{5}$$

in (4) has the property

$$\langle f|Tg\rangle = \left\langle m^* T\frac{f}{m}\middle| g\right\rangle \tag{6}$$

for quantum states $|f\rangle$ and $|g\rangle$. Therefore (5) is non-Hermitian making (4) no longer valid. Equation (4) must then be replaced with the effective mass Schrödinger equation [14]:

$$-\frac{\hbar^2}{2}\nabla\cdot\frac{1}{m^*}\nabla\psi + U\psi = E\psi\,. \tag{7}$$

This form contains a Hamiltonian that is Hermitian and reduces to (4) in the limit of a spatially independent effective mass. Using (7), the Kronig-Penny model of a semiconductor superlattice may be derived in a similar fashion to the traditional method of using (4) [13].

The calculated electron dispersion is shown in Fig. 12 for a 7 nm barrier system and a 1 nm barrier system. Energy is referenced with respect to the InAs conduction band edge. The dashed bands correspond to orbitals that overlap with the GaAs continuum; electrons at these energies therefore belong to the GaAs continuum and not the superlattice bandstructure. The bottom band corresponds to the calculated conduction band eigenstate as in Fig. 10. The second band in Fig. 12.a is not realized in the Atlas simulation due to its close proximity to the GaAs continuum (~0.59 eV). This is further exemplified in Fig. 12.b where the second band transitions from a bound to a scattering state.

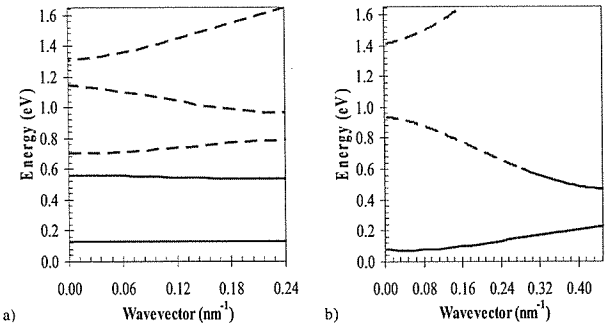

Fig. 12. Calculated electron dispersion in an InAs/GaAs superlattice for a) 7 nm GaAs barriers and b) 1 nm GaAs barriers. Dashed bands indicate orbitals that overlap with the GaAs continuum. Energy is referenced with respect to the InAs conduction band edge.

From Fig. 12, the width of the miniband is easily determined. This information is especially important for the intermediate band solar cell in which a fundamental requirement is that the intermediate band be half-filled with electrons [15]. The miniband width is plotted as a function of barrier thickness in Fig. 13. Decreasing barrier widths gives rise to an asymptotic increase in miniband width due to enhanced well-to-well coupling brought about by stronger wavefunction overlaps.

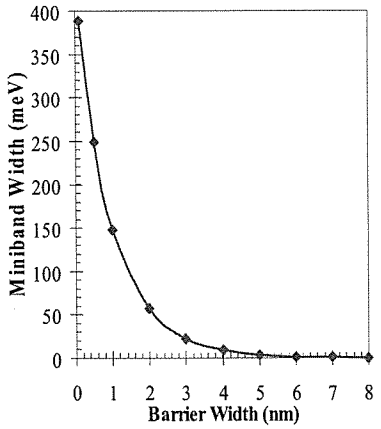

Fig. 13. The decrease in barrier width gives rise to an asymptotic increase in the width of the miniband. This is due to the larger degree of wavefunction overlap that occurs for ever decreasing barrier widths.

VI. Conclusion

The modeling of novel photovoltaic devices based on nanostructure arrays has been undertaken. The specific system investigated here was the incorporation an InAs quantum dot array in a GaAs host. For device simulations, the InAs quantum dots were approximated as quantum wells for the sake of invoking an available model.

Justification for doing so was given and viable results were obtained.

The ability to simulate a baseline device was presented and allowed for further simulation with the inclusion of the nanostructured arrays. Although an appropriate model for quantum mechanical charge carrier photogeneration was not identified, basic quantum effects were adequately simulated and analyzed. As an extension to this, bandstructure calculations were performed based on an effective mass Kronig-Penny model. With these analysis methods, optimization of the nanostructured arrays are now possible and will lead way to more efficient photovoltaic devices.

ACKNOWLEDGEMENTS

The author would like to thank Dr. R. Raffaelle, Dr. S. Hubbard, and Dr. S. Rommel for their continued advice. He would also like to acknowledge Dr. C. Cress and Dr. J. Andersen for illuminating discussions and assistance. Device simulations were made possible by the donation of the Silvaco tools by Simucad Design Automation to the Microelectronic Engineering Dept.

REFERENCES

[1] W. Shockley and H. J. Queisser, "Detailed Balance Limit of Efficiency of p-n Junction Solar Cells," *J. Appl. Phys.*, vol. 32, pp. 510-519, 1961.

[2] A. De Vos, "Detailed Balance Limit of the Efficiency of Tandem Solar Cells," *J. Phys. D*, vol. 13, pp. 839-846, 1980.

[3] R. R. King, D. C. Law, K. M. Edmondson, C. M. Fetzer, G. S. Kinsey, H. Yoon, R. A. Sherif, and N. H. Karam, "40% Efficient Metamorphic GaInP/GaInAs/Ge Multijunction Solar Cells," *Appl. Phys. Lett.*, vol. 90, pp. 183516-1–183516-3, 2007.

[4] R. P. Raffaelle, S. Sinharoy, J. Andersen, D. M. Wilt, and S. G. Bailey, "Multi-Junction Solar Cell Spectral Tuning with Quantum Dots," in *Conf. Rec. 2006 IEEE 4th World Conf. Photovoltaic Energy Conv.*, Waikoloa, HI, 2006, pp.162-166.

[5] National Renewable Energy Laboratory: Renewable Resource Data Center, "Solar Spectra: Air Mass Zero," May 2008; http://rredc.nrel.gov/solar/spectra/am0/.

[6] K. W. J. Barnham and G. Duggan, "A New Approach to High-Efficiency Multi-Band-Gap Solar Cells," *J. Appl. Phys.*, vol. 67, pp. 3490-3493, 1990.

[7] A. Martí, L. Cuadra, and A. Luque, "Quantum Dot Intermediate Band Solar Cell," in *Conf. Rec. 28th IEEE Photovoltaics Spec. Conf.*, Anchorage, AK, 2000, pp. 940-943.

[8] A. Luque and A. Marti, "Increasing the Efficiency of Ideal Solar Cells by Photon Induced Transitions at Intermediate Levels," *Phys. Rev. Lett.*, vol. 78, pp. 5014-5017, 1997.

[9] *Atlas User's Manual*, Silvaco, Satan Clara, CA, 2008.

[10] A. Ioannides, T. N. D. Tibbits, J. P. Connolly, D. B. Bushnell, K. W. J. Barnham, C. Calder, G. Hill J. S. Roberts, and G. Smekens, "Strain Balanced Quantum Well Monolithic Tandem Solar Cells," in *Conf. Rec. 2006 IEEE 4th World Conf. Photovoltaic Energy Conv.*, Waikoloa, HI, 2006, pp.753-756.

[11] A. Martí, N. López, E. Antolín, E. Cánovas, A. Luque, C. R. Stanley, C. D. Farmer, and P. Díaz, "Emitter Degradation in Quantum Dot Intermediate Band Solar Cells," *Appl. Phys. Lett.*, vol. 90, pp. 233510-1–233510-3 , 2007.

[12] N. López, A. Martí, A. Luque, C. Stanley, C. Farmer, and P. Diaz, "Experimental Analysis of the Operation of Quantum Dot Intermediate Band Solar Cells," *J. Solar Energy Engineering*, vol. 129, pp. 319-322, 2007.

[13] C. Kittel, *Introduction to Solid State Physics*, 8th Ed. John Wiley & Sons, 2005.

[14] S. Datta, *Quantum Phenomena*, Addison-Wesley Publishing Co., 1989.

[15] A. Martí, L. Cuadra, and A. Luque, "Patial Filling of a Quantum Dot Intermediate Band for Solar Cells," *IEEE Trans. Elec. Devices*, vol.48, pp. 2394-2399, 2001.

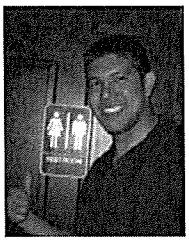

Ryan Aguinaldo received the BS degree in microelectronic engineering, with minors in physics and electrical engineering, and the MS degree in materials science, concurrently, from the Rochester Institute of Technology in 2008. His interests lie in the broad areas of applied physics, device electronics, and quantum phenomena.

In 2005 he interned as a research assistant at the College of Nanoscale Science and Engineering, State University of New York – Albany where he investigated optical gas sensing by means of porous silicon distributed Bragg reflectors. In 2006 he served as a process engineer for International Business Machines, East Fishkill, NY in the 300 mm ion implant sector. Since 2005 he has been a research assistant for the Nanopower Research Laboratories where he worked primarily on the modeling of III-V nanostructured photovoltaic devices.

Mr. Aguinaldo will pursue the PhD degree in electrical engineering at the University of California – San Diego beginning in the autumn of 2008.